International Communications in Heat and Mass Transfer 148 (2023) 107046

Contents lists available at ScienceDirect

International Communications in Heat and Mass Transfer

journal homepage: www.elsevier.com/locate/ichmt

Experimental indirect cooling performance analysis of the metal 3D-printed cold plates with two different supporting elements

Baris Burak Kanbur [a,b,*], Mun Hoe Seat [b], Wiebke Brix Markussen [a,c,**], Martin Ryhl Kærn [a,d], Fei Duan [b,**]

[a] Department of Mechanical Engineering, Technical University of Denmark, Nils Koppels Allé, Building 403, Copenhagen 2800, Denmark
[b] School of Mechanical and Aerospace Engineering, Nanyang Technological University, 50 Nanyang Ave, Block N3, Singapore 639798, Singapore
[c] Center of Refrigeration and Heat pump Technology, Danish Technological Institute, Gregersensvej 1, Copenhagen 2630, Denmark
[d] Thermodynamics and Energy Technology, IPU, Bredevej 2B, Copenhagen 2830, Denmark

ARTICLE INFO

Keywords:
Cold plate
Thermal management
Indirect cooling
Metal 3D printing

ABSTRACT

This study experimentally investigates the cooling time and performance of two new cold plate designs manufactured via selective laser melting process using body-centred cubic (BCC) and pillar elements. The plates are cooled down from the initial surface temperature of 45 °C to the target surface temperature of 32.5 °C under tropical conditions at three different volume flow rates and two different inlet water temperatures. The minimum cooling time is found at 30 s and 63 s at the highest volume flow rate and the lowest inlet water temperature for the pillar- and BCC-filled plates, respectively. The greatest plate and system COP values are 1195.1 and 6.8 for the BCC-filled plate and 1192.0 and 6.2 for the pillar-filled plate, respectively, at the minimum flow rate and the inlet water temperature. The performance evaluation criterion range is 1.25 to 1.28 and 2.12 to 2.52 for the BCC- and pillar-filled plates, respectively. The heat transfer coefficient dramatically increases by rising the volume flow rate at the low inlet water temperature case but the increasing trends become slighter at the high inlet water temperature case. Tropical climate results in high dew point temperatures, therefore, cooling with high inlet water temperature is found ineffective.

1. Introduction

Indirect liquid cooling (ILC) applications are being preferred in the thermal management of power sources and batteries as they provide longevity and low risk of leakage despite they bring some drawbacks like causing greater pressure drops and less efficiency (or the coefficient of performance (COP)) due to the additional thermal resistance layer between the heat source and the coolant [1,2]. Cold plates are the most common ILC solutions in battery thermal management systems (BTMSs) for electric vehicles (EVs) [3] as they have a lower risk of leakage, scalability for various sizes/capacities, and easy maintenance options while another common ILC method, heat pipes may encounter challenges due to its complex design characteristics and performance limitations [4,5] that can rise safety-related concerns during the dynamic operating conditions of the EVs. Cold plates can be applied in both two-phase and single-phase cooling operations. For the high heat flux operations, which can be defined as the heat flux rates above 1 W/cm^2, the cold plates have been operated for two-phase cooling purposes [6,7], particularly for the thermal management of electronics and microprocessors. On the other hand, the vast majority of the lab-scale cold plate studies for the BTMS were performed with single-phase cooling operations as they were able to remove the generated heat rate without a two-phase cooling requirement. For example, Zhao et al. [8] successfully managed the thermal gradients and cooling performance of the lithium batteries with the heat generation rate of 24,000 W/m^3, but it was also seen that higher volume flow rates were required for keeping the thermal gradients in the desired operating conditions.

From the past to the present, both experimental and numerical efforts have been done for investigating the cooling performance of cold plates in thermal management applications. Cooling time, thermal uniformity on the battery surface, COP (or other relevant performance indicators), and pressure drop have been the main considerations while evaluating cold plate performance. Also, not at the lab scale but for the

* Corresponding author at: Technical University of Denmark, Denmark.
** Corresponding authors.
E-mail addresses: babukan@dtu.dk, bbkanbur@ntu.edu.sg (B.B. Kanbur), mseat001@e.ntu.edu.sg (M.H. Seat), wb@mek.dtu.dk, wbm@teknologisk.dk (W.B. Markussen), pmak@mek.dtu.dk, mrk@ipu.dk (M.R. Kærn), feiduan@ntu.edu.sg (F. Duan).

https://doi.org/10.1016/j.icheatmasstransfer.2023.107046

Available online 30 September 2023

Nomenclature

A	Area (m^2)
C_p	Specific heat (kJ/kgK)
D_h	Hydraulic diameter (m)
E	Volume (or area)-reduced power input (W/m^3 or W/m^2)
f	Friction factor (−)
h	Convective heat transfer coefficient (W/m^2K)
k	Thermal conductivity (W/mK)
L	Length of the heat transfer (fluid flow) surface (m)
$\dot{m}$	Mass flow rate (kg/s)
Nu	Nusselt number (−)
P	Pressure (Pa)
q	Heat flux (W/m^2)
Pr	Prandtl Number (Pr)
q	Heat flux (W/m^2)
Q	Heat rate (W or kW)
Re	Reynolds number (−)
t	Time (s)
T	Temperature (K)
u	Velocity (m/s)
U	Overall heat transfer coefficient (W/m^2K)
V	Volume (m^3)
$\dot{V}$	Volume flow rate (m^3/s)
δR	Overall uncertainty
∂X_i	Uncertainty of X for variable i
$\frac{\partial R}{\partial X_i}$	Sensitivity of the coefficient for δR

Subscripts

amb	Ambient environment
bath	Water bath
d	Dissipated
flow	Flow-related
max	Maximum
plate	Cold plate
ref	Reference
surf	Surface
system	Cooling system
w	Water
wall	Cavity wall
w,in	Water inlet
w,out	Water outlet

Greek letters

η_0	Extended surface efficiency (−)
ε	Heat exchanger effectiveness
μ	Dynamic viscosity (Pa · s)
ρ	Density (kg/m^3)
σ	ratio of free flow area to the frontal area (−)

Abbreviations

D	Three-dimensional
BCC	Body-centred Cubic
BTMS	Battery Thermal Management System
COP	Coefficient of Performance
EV	Electric Vehicle
ILC	Indirect Liquid Cooling
NTU	Number of Heat Transfer Units
PEC	Performance Evaluation Criterion
VGF	Volume Goodness Factor

pilot- or real-scale battery packs, the weight has become another criterion [9]. Most of the conducted studies were based on commercial computational efforts [10] and design ideas [11]. Differently from the computational and optimization studies, the experimental works have been limited due to the difficulties of manufacturing newly-designed channel structures in the plate and managing the operating conditions, while the computational tools have allowed a more flexible environment for various design and operating alternatives. One of the recent experimental studies has been carried out by Wang et al. [12]. An aluminum cold plate was formed with a thickness of 1 mm for thermal management of a dummy battery with dimensions of 235 mm × 155 mm. Both heating and cooling scenarios were worked with the experimental periods of 600 s and 900 s, respectively. The volume flow rate was nearly 16.8 L/h. It was seen that the designed plate was able to keep the surface thermal gradients less than 5 K up to the ambient temperature of 45 °C. A greater flow rate range, from 0.01 kg/s to 0.03 kg/s, was applied by *Ma* et al. [13] for a cold plate with a U-type design. Depending on the applied flow rate, the pressure drop was found in the range of 300 Pa to 2750 Pa while the heat transfer coefficients were varied between 5000 W/m^2K to 20,000 W/m^2K when the inlet coolant (water) temperature was constant at 20 °C. In the flow rate range of 0.05 kg/min to 0.45 kg/min, Salimi et al. [14] calculated the same heat transfer coefficient range, from 5000 W/m^2K to 20,000 W/m^2K while the measured pressure drop was in between 200 Pa and 600 Pa for a straight channel-drilled cold plate with the inlet coolant temperature of 20 °C. Sun et al. [15] designed six different cold plate types with respect to the flow channel paths, fin structure, and coolant inlet/outlet locations. A processing unit with the heat generation rate of 300 W with the volume flow rate of 30 L/h to 90 L/h. The study showed the opposite trends between the cooling performance and pressure drop, which were both significant performance indicators during the design and optimization stages. A similar volume flow range rate (36 L/h to 90 L/h) was applied by Om et al. [16] to manage a battery pack with a thermal power rate of 300 W. Three different fin types, which were inlined, inclined, and louvered, were implemented in the cold plate and the target surface temperature was aimed at 45.0 °C. At various flow rates, the louvered channel achieved better performance. To find a trade-off between the trends of pressure drops and heat transfer rate, Li et al. [17] carried out a topology optimization for a cold plate design with dimensions of 55 mm × 55 mm. The results were compared to the traditional serpentine plate design. It was found that the pressure drop did not have a remarkable effect at low Reynolds numbers (e.g. 200); however, the optimized flow path was able to decrease the thermal resistance by 2.8 to 4.0 times at high Reynolds numbers. By using the plate dimensions of 160 mm × 210 mm, Kalkan et al. [18] performed cooling experiments with two different cold plate designs that were the mini channel and the serpentine channel. The inlet water temperature range of 15.0 °C to 35.0 °C was applied in the experiments with the volume flow rate range between 6 L/h and 66 L/h. Even though the mini channel design had a greater heat transfer surface area than the serpentine channel, neither the mini channel nor the serpentine channel types were not able to keep the battery surface temperature below 40.0 °C when the minimum flow rate was applied at high battery discharge rates.

The experimental cold plate studies were also performed with hybrid cooling options. Cao et al. [19] achieved keeping the battery surface temperature below 50.0 °C by applying a relatively high inlet coolant temperature, which ranged between 30.0 °C and 40.0 °C, thanks to integrating nano phase change material emulsions into the cooling flow that had a volume flow rate of 10 L/h for a cold plate with dimensions of 440 mm × 125 mm. Another phase change material-integrated cold plate solution was proposed by Akbarzadeh et al. [20]. A battery pack with a length of 400 mm and cross-sectional dimensions of 4 mm × 6 mm was presented to perform side cooling for 12 batteries at the same time. Phase change materials were implemented among the straight-

drilled plate channels so that the cooling operation was carried out in hybrid mode. It was seen that the proposed hybrid approach was able to save energy by up to 40% compared to the traditional plate design. Instead of integrating phase change material emulsions, Nada et al. [21] used two different nanoparticles in the circulated flow with the volume flow rate of 36 L/h to 72 L/h and the inlet coolant temperature of 21.0 °C. Three different flow paths were investigated serpentine, wavy, and parallel arrangements. Among others, the serpentine flow path reached the best thermal performance whereas the integration of the nanofluid decreased the thermal resistance by 6% to 25%. Considering all flow arrangements and the nanofluid operations, the range of the heat transfer effectiveness (ε) varied between 0.04 and 0.21. Apart from the hybrid cooling operations, Li et al. [22] increased the heat transfer surface area by implementing an aluminum foam structure with the porosity of 88% to a cold plate that had the dimensions of 45 mm × 75 mm × 13 mm. At nine different flow rates, the Reynolds number ranged from 500 to 1600. Even though the heat transfer performance was enhanced up to 1.8 times, the complex structure of the foam resulted in a large pressure drop, which made the solution less preferable compared to other approaches.

The above-mentioned experimental studies have been based on conventional designs (e.g. serpentine, parallel) or basic designs (e.g. wavy) that can be manufactured via traditional machining processes, while more complex designs including the additive-manufactured ones have been investigated under computational domains [23,24]. Recently, the metal three-dimensional (3D) printing concept has been becoming preferable in the manufacturing of heat exchangers as metal 3D printing can produce more complex designs with flexible contact surfaces [25]. Therefore, this study presents new cold plate designs with two different supporting elements that are BCC lattices and pillar elements. The supporting elements fill a large cooling cavity design inside the cold plate. Hereby, the metal 3D-printed plates aim at increasing the cooling performance and shortening the cooling time while managing the pressure drop with a greater heat transfer surface area compared to the traditionally-manufactured plates. Even though metal 3D printing allows us to present more complex flow patterns in the cooling cavity, the presented designs can still be considered basic designs with respect to the unique capabilities of the metal 3D printing processes. Thereby, the results of the current study do not only present results for two different plates but can also be used as the benchmark results for more complex cold plate designs manufactured via metal 3D printing. To this end, the main contributions of the study are i) experimental investigation of two new cold plate designs manufactured via metal 3D-printing process, ii) applying three different volume flow rates and two different inlet

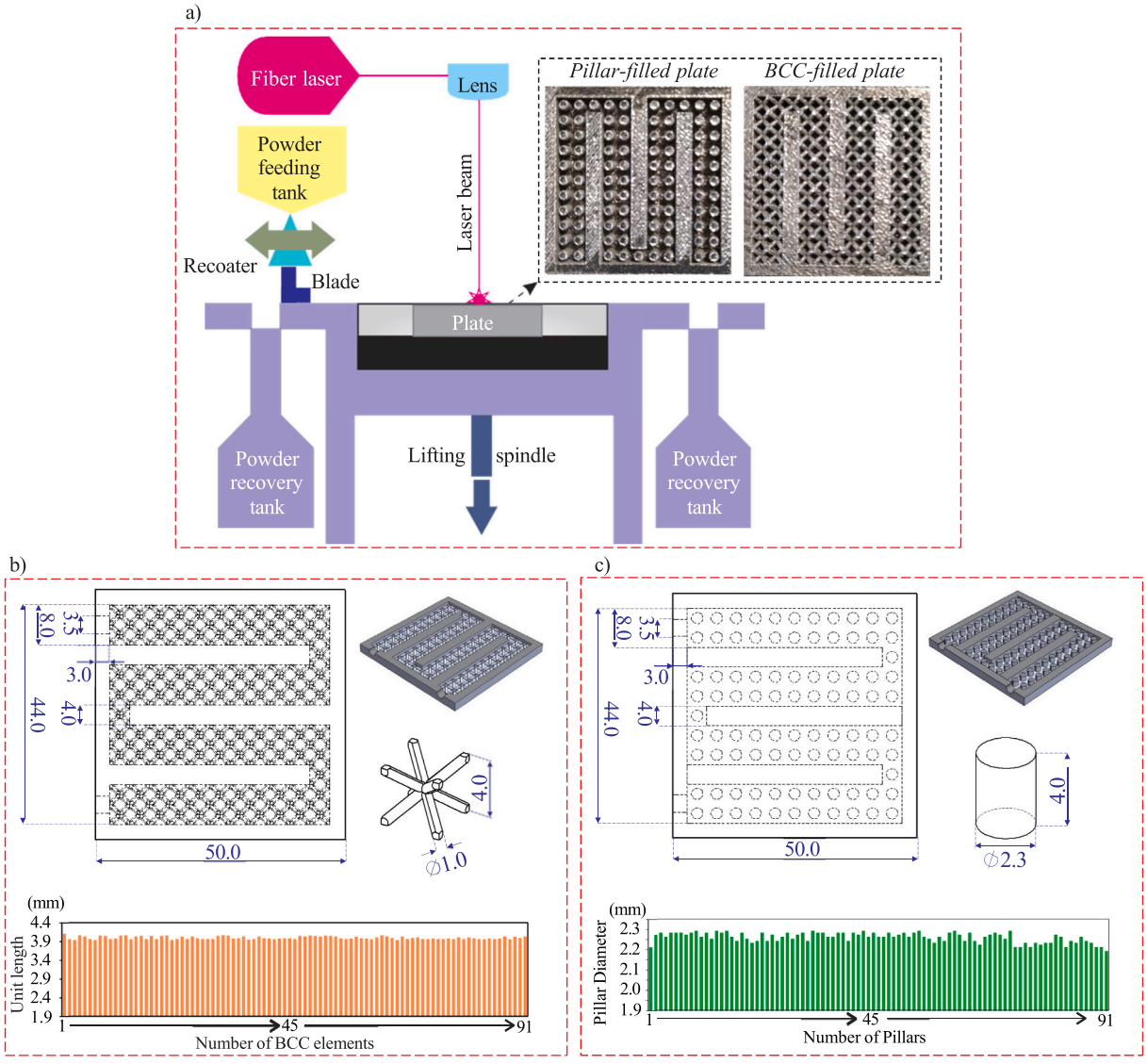

Fig. 1. Metal additive manufacturing process of the cold plates; a) selective laser melting process, b) BCC-filled plate specifications, and c) pillar-filled plate specifications.

coolant temperatures that are above and below the dew point temperatures, respectively, and iii) observing the cooling performance under tropical conditions that bring high relative humidity and ambient temperature. More details on the given contributions can be seen in the following sections.

2. Metal 3D printing of the cold plates

The metal 3D printing process was completed in the selective laser melting machine at the Singapore Centre for 3D Printing (SC3DP) as shown in Fig. 1a. The selective laser melting machine could print a product with a minimum feature size of 0.15 mm. The cold plates were manufactured with the printing parameters of i) diagonal scanning with 45° and ii) rotated layout of 5° with reference to our previous printing settings that were able to print reliable final products [26]. Four main stages of printing a metal product via selective laser melting are as follows: 1) the three-dimensional model of the product was sliced into the stack of two-dimensional layers, 2) the two-dimensional cross-sectional area was scanned via laser scanning, 3) the metal powders were spread on the finished layer, and 4) a new cycle was initiated until the target product was formed. The cold plates were printed by SS316L powders with the specific heat of 476.0 kJ/kgK and the thermal conductivity of 12.6 W/mK [27]. The top (and open) views of the cold plates can be seen in Fig. 1a. The external dimensions of the cold plates were 50 mm × 50 mm × 6 mm. The purpose of metal 3D-printed heat transfer surfaces was to increase the cooling performance and provide lightweight designs while managing the pressure drop during the cooling operation, as already discussed and presented by Liang et al. [28] in detail. Therefore, we proposed a large cooling cavity area with solid partitions inside the cold plate design. The cooling cavity dimensions were 44 mm × 44 mm × 4 mm for both BCC-filled and pillar-filled plates as shown in Figs. 1b and c, respectively. The main reason for creating solid partitions in the cooling cavity was to avoid printing failures and provide safe printing conditions, which fully depended on the machine's capabilities and the printing parameters. For each plate, there were three solid partitions with a thickness of 3 mm. Between the solid partitions and the cavity wall, two supporting elements were located in a row. In total, both BCC- and pillar-filled plates had 91 supporting elements. The BCC element had a strut diameter of 1.0 mm and a length of 4.0 mm (Fig. 1b) whilst the pillar element had a diameter of 2.3 mm and a length of 4.0 mm (Fig. 1c). Even though the shapes and geometries were different for the elements, both elements had very close total volume to each other; the volume of a single BCC element was 16.9 mm^3 whereas the pillar element had a volume of 16.6 mm^3. Based on the volumes of the elements, the BCC- and pillar-filled plates had a total surface area in the cavity (flow) volume of 9.3×10^{-3} m^2 and 6.7×10^{-3} m^2, respectively. That is, even though both elements had close volumes to each other, the BCC elements presented a larger heat transfer surface area as their curves and shapes had greater surface area than the pillar elements. Considering the height of the cavity and the lengths of the elements, both elements were in touch with both side surfaces of the cooling cavity because they have the same length/height. By using an image processing tool [29] after the printing, the unit lengths of the manufactured BCC elements were measured at 4.0 ± 0.1 mm while the pillar diameter of the pillar elements was 2.30 ± 0.02 mm. Both element types were in good agreement with the designed value. Also, the surface roughness of the cooling cavity surface was measured to be 2.60 ± 0.02 μm (via Confocal Microscopy, Leica DCM). Moreover, both plates had circular inlets and outlets with a diameter of 3.5 mm.

3. Experimental setup

A lab-scale experimental setup was used in this study. As shown in Fig. 2a, a Teflon housing covered the setup to prevent heat losses to the ambient environment. The setup had a heater, two heated plates, two cold plates, and two insulation plates (to block heat loss from the side

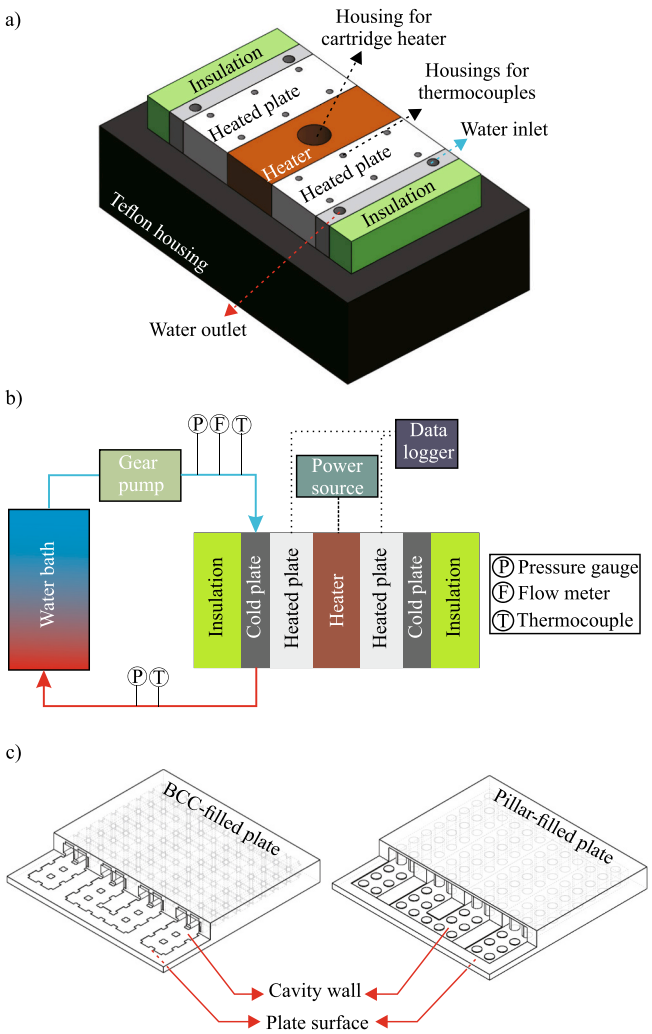

Fig. 2. The experimental setup; a) three-dimensional view of the housing, b) simplified diagram, and c) cavity wall and plate surface of the cold plates.

surfaces of the cold plates). The copper heater had housing for a cartridge heater with a maximum capacity of 300 W, and it was connected to the power source (Fig. 2b). In the study, we supplied a constant heat flux of 1049.1 ± 44.9 W/m^2, which was continuously measured by the calibrated heat flux sensor (Hukseflux FHF03–05, the Netherlands). The selected constant heat flux rate was in good agreement with the heat fluxes in the previously performed BTMS studies [3,12,30,31]. On both sides of the heater, two aluminum plates were located as the heated plates. Those plates transferred the generated heat from the heater to the cold plates through adjacent surfaces (plate wall, Fig. 2c). Each heated plate had six thermocouples (J-type, accuracy of 0.4 °C) with two rows; each row had three thermocouple housings. Using multiple thermocouples at different rows in a single heat plate aimed at i) collecting multiple temperature data, ii) observing the thermal uniformity on the surface, and iii) providing backup measurements in case of single or multiple thermocouple failures. In the experiments, based on the collected temperature data, there were no significant temperature differences; therefore, the heat flux was assumed uniform on the plate surface. Each heated plate represented a heated battery (or power source) surface under the constant heat flux; thus, the cold plate was operated to cool down the heated surface by circulating a coolant inside the cooling cavity (cavity wall, see Fig. 2c) while other external sides of the plates were adjacent to insulation materials. Thereby, there was no measured heat loss from those sides. Two cold plates could be operated by using the setup as there were two heated plates. However, in the

current study, we operated only one of the cold plates with the constant heat flux of 1049.1 ± 44.9 W/m^2 while the other plate was not connected to the water bath as shown in Fig. 2b. The coolant was circulated between the cold plate and the water bath whereas the pressure and temperature data were collected at both inlet and outlet of the cold plate. The pressures and temperatures were measured via mechanical pressure gauges (accuracy of 50 Pa) and J-type thermocouples (accuracy of 0.4 °C), respectively. Also, the volume flow rate was measured with a variable area flow meter (accuracy of 0.1 L/h). The water tank was an insulated body; filled with the city water of Singapore with the approximate temperature of 26.3 °C. The COP of the refrigeration system cooling the water bath was 3.5 in the operating (filled water) temperature range of 0 °C to 30.0 °C. Using the sensitivity values of the measurement devices, the propagated uncertainty can be calculated with Eq. 1,

$$\delta R = \left[\sum_{i=1}^{N}\left(\frac{\partial R}{\partial X_i}\delta X_i\right)^2\right]^{1/2} \quad (1)$$

where δX_i and δR are the uncertainty value for variable i and the overall uncertainty, respectively. The sensitivity coefficient for the R with respect to X is defined as $\frac{\partial R}{\partial X_i}$ [32]. Table 1 shows the calculated uncertainty values for the measurements below,

The experimental setup in Fig. 2 had a partially open surface to the ambient environment from a small portion of the lateral sides and the entire top surface. Considering the ambient conditions in the tropical climate, the ambient air inherently brought challenges and limitations for the cooling operation; therefore, the operating parameters were defined with respect to those limitations. During the experimental period of more than one and half months, the ambient temperature varied between 26.8 °C and 28.9 °C whereas the relative humidity was in the range of 70% to 80% on different days. Corresponding to the ambient conditions, the dew point temperature range was roundly between 22.0 °C and 24.0 °C. Therefore, during the design of the experimental procedure, the target (cooled down) surface temperature was defined as 32.5 °C, which was above the ambient conditions and in the acceptable range of the battery operating temperatures that was in between 15.0 °C and 35.0 °C [33]. Similar to the first scenario of Ref. [20], the (heated) surface was heated up to the initial surface temperature of 45 °C; then, the cooling mode was activated at the constant heat flux supply. It is worth noting that the experimental campaign aimed to reach steady-state conditions neither the heating process till reaching the initial surface temperature nor the cooling process till reaching the target surface temperature. After reaching the target surface temperature, the cooling process was stopped; hence, each experimental set had different cooling time values without reaching the steady state conditions. To decrease the surface temperature, two different inlet water temperatures were applied i) inlet temperature below the dew point (condensation) temperature and ii) inlet temperature above the dew point temperature. The reason for choosing two different inlet temperatures below and above the dew point temperature was to see the potential impacts of the condensation layer, which occurred on the cold plate surface when the inlet coolant temperature was below the dew point temperature. For the BCC-filled plates, the low and high inlet water temperatures were 15.8 ± 0.3 °C and 24.6 ± 0.1 °C, respectively. On the other hand, the low and high inlet temperatures were 15.7 ± 0.4 °C and 24.6 ± 0.1 °C for the pillar-filled plate. Even though we tried to obtain the inlet temperature values for the BCC- and pillar-filled plates as closely as possible, we had still quite a difference for the low inlet water temperatures while the high inlet water temperatures were the same for both plates. The experiments were also performed under different flow rates, which were low-level, medium-level, and high-level flow rates for the plates. The BCC- and pillar-filled plates did not have the same flow rates at the medium- and high-level flow rate levels, but the values were quite close to each other at the low flow rate levels. For the BCC-filled plate, the low-, medium- and high-level flow rates were 3.4 L/h, 6.8 L/h, and 8.2 L/h, respectively. For the pillar-filled plate, the low-, medium- and high-level flow rates were 3.4 L/h, 7.1 L/h, and 8.7 L/h, respectively. The measured pressure drops at different flow rates are shown in Fig. 3a. Each experimental set was repeated three times so the error bars of the measurements were created based on the repeated experiments. From the initial surface temperature to the target surface temperature, the temperature data was collected every 2 s; then, cooling trends were generated by using the collected temperature data. As a representative plot, Fig. 3b shows different cooling trends with respect to various inlet water temperatures based on the selected experiments. The ambient air velocity above the experimental setup was 3 m/s, measured by a velocity anemometer. It is worth mentioning that the experimental campaigns were not performed at steady conditions. It only focused on the duration of active cooling time from the initial surface temperature to the target surface temperature as represented in Fig. 3b. This simply means that different parametric sets had different cooling times so the constant time duration-based analysis was not considered in the methodology. Instead, for each experimental set, the time-averaged performance analysis was used by considering the time from the initial surface temperature to the target surface temperature.

Table 1
Uncertainty of measurement in the experimental setup.

Parametric set	Uncertainty
Flow rate	0.1 L/h
Pressure in the flow loop	70.7 Pa
Temperature in each row of the aluminum heated plate	0.7 °C
Temperature in the flow loop	0.6 °C

4. Method

The thermal performance of the cold plates was calculated by using the measured data and building a heat transfer model as projected in

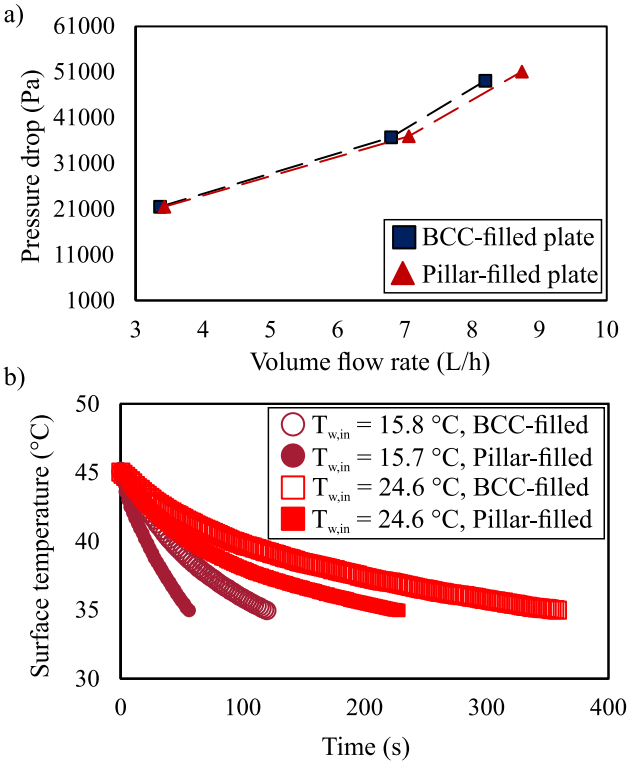

Fig. 3. Experimental setup measurements; a) pressure drop trends and b) cooling time trends at the low-level volume flow rate.

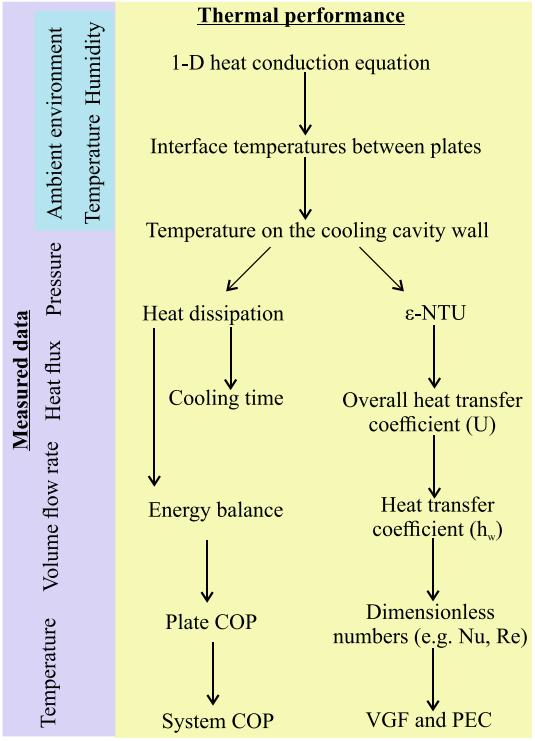

Fig. 4. Flow of the model for thermal performance analysis.

Fig. 4. The measurement devices and sensors on the experimental setup continuously collected data sets for pressure, temperature, heat flux, and volume flow rate whereas the ambient conditions (temperature, relative humidity, and air velocity above the setup) were measured. One-dimensional conductive heat transfer was assumed from the heater to the cold plate; thus, Fourier's heat transfer equation was used to calculate the plate surface temperature (T_{surf}), which was already shown in Fig. 2c, thanks to the collected temperature and heat flux data. The cooling mode was activated when T_{surf} reached 45 °C. In parallel to the calculation of T_{surf}, the cavity wall temperature (T_{wall}), shown in Fig. 2c as well, was also calculated by using the one-dimensional conductive heat transfer equation. However, the calculation of T_{wall} was based on two main assumptions. The first assumption, which is a very common and given in detail in Ref. [34], was that all the walls in the cooling cavity had the same temperature. The second assumption was that the surfaces of all supporting elements in the cooling cavity had the same temperature as the cavity wall temperature (T_{wall}), because the lengths of the supporting elements were small (4 mm) and the SS316L had a high thermal conductivity, thermal gradients on the surfaces of the supporting elements were neglected, which was similar to the fin modeling study by Om et al. [16]. The heat transfer performance was analyzed with the convective heat transfer coefficient (h_w). To find the h_w term, the epsilon -number of transfer units (ε-NTU) method was preferred. The current plate had a single flow stream and heat exchange process. Thus, the NTU is presented in Eq. 2,

$$NTU = ln\frac{1}{1-\varepsilon} \tag{2}$$

where ε infers the effectiveness, which is the ratio of the heat flux in the plate (q) to the maximum heat flux (q_{max}). Shah and Sekulić [35] defined the ε term based on the temperature ratio for the single heat exchange process as given in Eq. 3,

$$\varepsilon = \frac{T_{w,out} - T_{w,in}}{T_{wall} - T_{w,in}} \tag{3}$$

Calculating the NTU term allowed us to define the overall heat transfer coefficient, U, as shown in Eq. 4,

$$\mathrm{U} = \frac{NTU \cdot A}{\dot{m}_w \cdot C_{p,w}} \tag{4}$$

where $\dot{m}_w$ is the mass flow rate, which can be calculated from the volume flow rate, $\dot{V}$, of the experimental study. The specific heat capacity of the coolant (water) is denoted by $C_{p,w}$ whilst the heat transfer surface area in the flow volume is shown with A. For the BCC- and pillar-filled plates, the A was 92.82 cm^2 and 66.70 cm^2, respectively. After defining the U value, the h_w term is found with Eq. 5,

$$\frac{1}{U \cdot A} = \frac{1}{h_w \cdot A} + \frac{L_{wall}}{k \cdot A} \tag{5}$$

where L_{wall} is the length of the heat transfer surface from the plate surface to the cavity wall surface, and k is the thermal conductivity. The second term on the right hand side of Eq. 5 was not considered in the current work as the U value was determined by T_{wall} in Eq. 4. In case of using T_{surf} measurements instead of calculating T_{wall}, the term of heat conduction resistance can be used; both approaches gave the same results for calculation of h_w. Dimensionless numbers such as the Reynolds number (Re) and the Nusselt number (Nu) are later calculated as given in Eqs. 6 and 7, respectively,

$$Re = \frac{\rho_w \cdot u_w \cdot D_h}{\mu_w} \tag{6}$$

$$\mathrm{Nu} = \frac{h_w \cdot D_h}{k_w} \tag{7}$$

where ρ_w, μ_w, k_w, and u_w are the density, dynamic viscosity, thermal conductivity, and velocity of the water, respectively. The hydraulic diameter is denoted by D_h and it is explained for the extended surfaces as shown in Eq. 8,

$$D_h = \frac{4V_{flow}}{A} \tag{8}$$

where V_{flow} denotes the core flow volume of the cold plates, which can be found from the computer-aided design model of the plate for each supporting element type. Besides the h_w and relevant heat transfer terms, the dissipated heat rate by the circulated water ($\dot{Q}_d$) is calculated using the measured temperature data. The $\dot{Q}_d$ term is defined in Eq. 9,

$$\dot{Q}_d = \dot{m}_w \cdot C_{p,w} \cdot \left(T_{w,out} - T_{w,in}\right) \tag{9}$$

Even though the setup was insulated from lateral surfaces using a Teflon housing (see Fig. 2a), there was still a heat gain from the high ambient temperature environment (due to the tropical climate) to the 3D-printed plates that circulated water inside. Therefore, two terms affected the $\dot{Q}_d$ term; i) heat gain from the heater, which was used for representing a battery surface, $\dot{Q}_{plate}$, and ii) heat gain from the high-temperature ambient environment, $\dot{Q}_{amb}$. Hence, the increase in flow rate or the decrease in water inlet temperature affects the share of these two terms in the $\dot{Q}_d$ term, which brings complexity to the understanding of cooling performance trends for all open-type (fully or partially) battery cooling packs in real environments.

Both h_w and $\dot{Q}_d$ have crucial roles in the performance analysis. In the study, three different performance indicators were used, which were the COP, the VGF, and performance evaluation criterion (PEC). The COP had two different definitions. The first COP defined the COP of the cold plate; thus it was denoted by COP_{plate}, while the second COP term considered the impact of the cooling load of circulated water between the cold plate and the water bath, which deduced the consumed energy rate to cool down the city water to the inlet water temperature; hence, the second COP term was named COP_{system}. The COP_{plate} and COP_{system} are shown in Eqs. 10 and 11, respectively,

$$COP_{plate} = \frac{\dot{Q}_d}{\dot{V}\cdot\Delta P} \tag{10}$$

$$COP_{system} = \frac{\dot{Q}_d}{\left(\dot{V}\cdot\Delta P\right) + \dot{W}_{bath}} \tag{11}$$

where ΔP denotes the pressure drop in the cold plate, and its trends are plotted in Fig. 3a. The required power rate to cool down the water in the water bath to the inlet water temperature is denoted by $\dot{W}_{bath}$ and explained in Eq. 12,

$$\dot{W}_{bath} = \frac{\dot{m}_w\cdot C_{p,w}\cdot\left(T_{bath} - T_{w,in}\right)}{COP_{bath}} \tag{12}$$

where T_{bath} is the accumulated water temperature in the water bath (26.3 °C) and the COP_{bath} was 3.5. To characterize the plate performances based on the varying parameters, a combined assessment term called Volume Goodness Factor (VGF) is considered. The VGF term was proposed by Shah and London [36], and it is a useful term to assess the heat transfer performance in the flow volumes where the cross-sectional area changes through the channel. It can be simple defined as the ratio of the heat transfer performance to the volume-reduced power by focusing the core flow volume as given in Eq. 13 [36,37],

$$VGF = \propto(\eta_0 h_w\beta, E\beta) \quad \text{for} \quad E\beta = \frac{4\cdot\dot{m}_w\cdot\Delta P\cdot\sigma}{\rho\cdot A\cdot D_h} \tag{13}$$

where $\propto$ refers to the dependency (functional relationship) of the VGF on the terms of $E\beta$ and $\eta_0 h_w\beta$. The extended surface efficiency is denoted by η_0 while the density of the heat transfer surface area is presented with β that can be defined as $\frac{4\cdot\sigma}{D_h}$ with reference to Shah and SekuliÄ‡ [35]. Since the VGF was defined with the core flow volume-related terms, the cooling performances of both plates can be assessed in a single plot, as discussed in the Results and Discussion section. The last performance indicator was the PEC, which compared the performance of the target product to the reference product by using the heat transfer performance (heat transfer coefficient) and the friction factor. In the current study, the target products were the newly-presented cold plates while the reference product was the cold plate with the same cooling cavity without any supporting element. The PEC term is defined in Eq. 14 [38],

$$PEC = \frac{Nu/Nu_{ref}}{\left(f/f_{ref}\right)^{1/3}} \tag{14}$$

where f denotes the friction factor and the subscript *ref* infers the cold plate without supporting elements. That is, the D_h term is constant along the cold plate surface since the plate had a constant cross-section profile as a rectangular duct shape. Therefore, the heat transfer calculations of the reference plate were completed by using the heat transfer correlations in Refs. [35] with respect to the operating parameters of the study (e.g. flow rate, heat flux, temperature). Similar to the VGF term, the PEC value also brought an opportunity to evaluate the performance of the cold plates in a single plot, but also gave a chance to compare with previously developed cold plates [21,22,39–43].

5. Results and discussion

The cooling time trends of the BCC-filled plate are shown for $T_{w,in}$ = 15.8 °C and $T_{w,in}$ = 24.6 °C in Fig. 5a and b, respectively. In Fig. 5a, it is seen that the cooling time trends had a large deviation bar (for repeated experiments) at the volume flow rate of 3.4 L/h in both for T_{surf} = 32.5 °C and T_{surf} = 35.0 °C, but the greatest deviation was seen for T_{surf} = 32.5 °C, which was a closer value to the ambient temperature. The average cooling time values were found 91 s and 143 s for T_{surf} = 35.0 °C and T_{surf} = 32.5 °C, respectively. Both 91 s and 143 s were acceptable duration according to the obtained cooling time values from previously

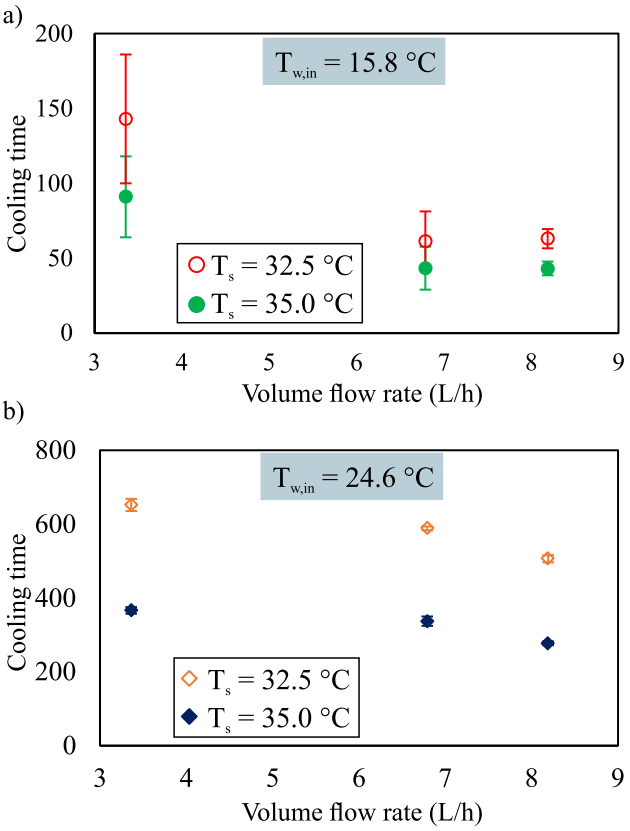

Fig. 5. Cooling time trends of the BCC-filled plate for a) $T_{w,in}$ = 15.8 °C and b) $T_{w,in}$ = 24.6 °C.

studied real-scale cooling pack solutions [44]. In order to decrease the surface temperature value to the desired values, but shorter duration were achieved with higher volume flow rates like 6.8 L/h and 8.2 L/h. At the volume flow rate of 6.8 L/h, the deviations significantly decreased while the minimum (and almost negligible) deviations were obtained at the volume flow rate of 8.2 L/h. When the volume flow rate was increased from 3.4 L/h to 6.8 L/h, the cooling time decreased by 57.1% and 52.4% for T_{surf} = 35.0 °C and T_{surf} = 32.5 °C, respectively; however, there was no dramatic change observed when the volume flow rate increased from 6.8 L/h to 8.2 L/h.For the trends of T_{surf} = 35.0 °C, the decrement rate was 2.3% while it was 3.2% for the trends of T_{surf} = 32.5 °C. It shows that operating the system with the volume flow rate of 8.2 L/h did not decrease the cooling time significantly but increased the energy consumption; hence, operating the setup with the volume flow rate of 6.8 L/h was a better idea compared to the operations with the volume flow rates of 3.4 L/h and 8.2 L/h. The reason behind observing small changes from 6.8 L/h to 8.2 L/h might be related to the interactions with the ambient environment, particularly from the top surfaces of the experimental setup. As explained in the paragraph just after Eq. 9 above, the changes in the flow rate and the water inlet temperature affected the shares of the heat gains from the heater plate and the high-temperature ambient environment. Thus, for the observed small changes from 6.8 L/h to 8.2 L/h, it can be speculated that further increment in the volume flow rate did not significantly affect the heat gain from the heater plate but increased the heat gain from the environment. Hence, the decrement rates were observed smaller compared to the decrement rates from 3.4 L/h to 6.8 L/h. Nevertheless, it is also possible to overreach this speculation with more detailed investigations of the experiments from the standpoints of i) experiments with larger plate sizes, ii) experiments under a fully controllable environment, iii) fully-insulated experimental campaign, iv) real-time observation of condensation layers on the 3D-printed surface, v) computational fluid

dynamics studies for fluid-solid interactions inside the plate.

Fig. 5b shows that the cooling time values were significantly high at $T_{w,in} = 24.6$ °C. For $T_{surf} = 35.0$ °C and $T_{surf} = 32.5$ °C, the cooling time was found 366.0 s and 651.3 s when the volume flow rate was 3.4 L/h. The increase of the volume flow rate from 3.4 L/h to 6.8 L/h achieved 8.0% to 10.0% decrements in the cooling time. At the volume flow rate of 8.2 L/h, the cooling time was measured 506.0 s and 277.0 s for $T_{surf} = 35.0$ °C and $T_{surf} = 32.5$ °C, respectively. It was also seen that the cooling time trends at $T_{w,in} = 24.6$ °C had almost zero deviations. That is, the volume flow rate was not the only parameter that can decrease the deviation; higher inlet water temperatures also minimized the deviations during the repeatable experiments. The main difference between the operation of the cooling setup with $T_{w,in} = 15.8$ °C and $T_{w,in} = 24.6$ °C was the dew point temperature. Considering the ambient air conditions, the dew point temperature was in the range of 22 °C to 24 °C. Thus, the operations with $T_{w,in} = 24.6$ °C were above the dew point while the operations with $T_{w,in} = 15.8$ °C were below, which resulted in a condensation layer on the cold plate surface and it had an impact on the occurred deviations during the temperature measurement.

Fig. 6a presents the cooling time trends of $T_{surf} = 35.0$ °C and $T_{surf} = 32.5$ °C for the pillar-filled plate at $T_{w,in} = 15.7$ °C. Similar to the BCC-filled plate, the largest deviation was at the minimum flow rate value, 3.4 L/h; the deviations for $T_{surf} = 32.5$ °C were higher than the deviations for $T_{surf} = 35.0$ °C. Compared to the BCC-filled plate, the pillar-filled plate had 43 s and 71 s shorter cooling time at the volume flow rate of 3.4 L/h, and even larger differences at higher flow rates. Behind observing a shorter cooling time trends for the pillar-filled plate, it can be speculated that the laminar vortex shedding behind the pillar elements, which improved the heat transfer and decreased the cooling time. To clarify, further design and analysis (e.g. different cooling cavity designs, and computational fluid dynamics simulations) can be applied. When the volume flow rate increased to 7.1 L/h, the cooling time decreased by 27.8% and 20.8% for $T_{surf} = 35.0$ °C and $T_{surf} = 32.5$ °C, respectively. When the flow rate increased to 8.7 L/h, and the minimum cooling time values were found 17.0 s and 30.0 s for $T_{surf} = 35.0$ °C and $T_{surf} = 32.5$ °C, respectively. The operation with $T_{w,in} = 24.6$ °C had also shorter cooling time trends than the trends of the BCC-filled plate as shown in Fig. 6b. Since there was no significant cooling time change from the flow rates of 7.1 L/h to 8.7 L/h, the volume flow rate of 7.1 L/h was the most convenient volume flow rate value. Also, as mentioned in BCC-filled plate trends, the operations below the dew point had higher deviations (e.g. $T_{w,in} = 15.7$ °C) due to the occurred condensation layer on the cold plate surface.

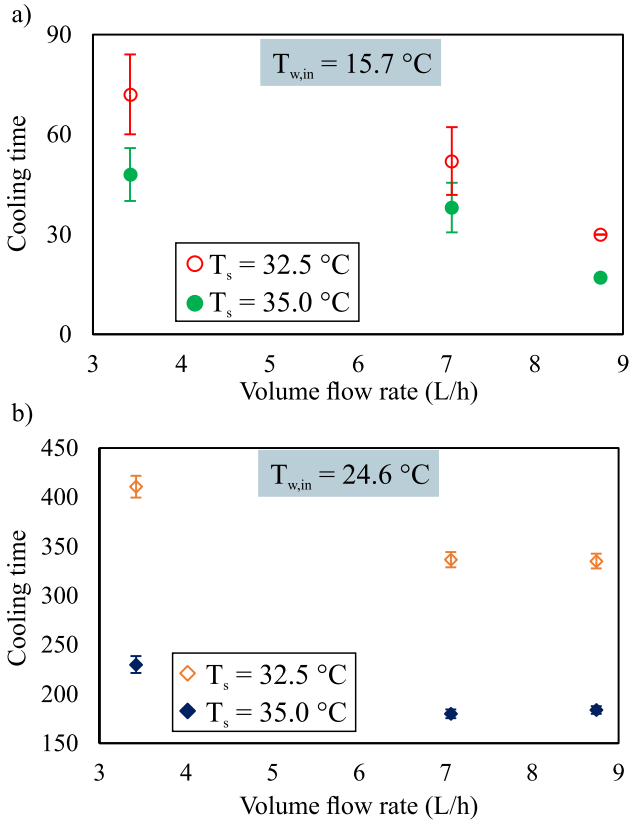

Fig. 6. Cooling time trends of the pillar-filled plate for a) $T_{w,in} = 15.7$ °C and b) $T_{w,in} = 24.6$ °C.

The mean values of the plate-level COP trends are projected for the BCC plate in Fig. 7a. The mean value was obtained by calculating the arithmetic average COP_{plate} value of the COP_{plate} trends along the experimental period. It is worth noting that the time average-based plotting was not performed at steady conditions; there-fore, does not represent constant time duration analysis. It covered the cooling period from the initial surface temperature to the target surface temperature, which was different in each experimental case. Hence, the plotted COP trends only give the average COP value during the cooling time; it does not give information to compare the reaction time of different parametric sets. The reaction of the parametric sets can be seen from the cooling time trends in Figs. 5 and 6. Apart from the time-dependent COP trends during the experimental period, the mean COP trends can give basic insights into the plate performance from the initial moment of the cooling to the end of the cooling. The mean value was obtained with an arithmetic average; therefore, simply present a single numeric value. The mean COP_{plate} trends decreased by rising the volume flow rate; however, the decrement rate varied with respect to the inlet water temperature. At $T_{w,in} = 15.8$ °C, from VFR = 3.4 to 8.2 L/h, the COP_{plate} decrements were 1.2 and 1.4 times lower for the $T_{surf} = 35.0$ °C and $T_{surf} = 32.5$ °C, respectively. The decrement rate at $T_{w,in} = 15.8$ °C was small compared to the decrement rates at $T_{w,in} = 24.6$ °C, which was 3.6 times lower for both $T_{surf} = 35.0$ °C and $T_{surf} = 32.5$ °C, respectively. The trends inferred that the increase of the volume flow rate did significantly affect the COP_{plate} at $T_{w,in} = 15.8$ °C and $T_{w,in} = 24.6$ °C. That is, the increment of the pressure drop term in Eq. 10 had a remarkable impact on the COP_{plate} calculations for any inlet water temperature value. Results also showed that the COP_{plate} trends at $T_{w,in} = 15.8$ °C for $T_{surf} = 32.5$ °C were slightly higher than the COP_{plate} trends of $T_{surf} = 35.0$ °C when the volume flow rate was 3.4 L/h, but that difference became nearly zero at the volume flow rate of 8.2 L/h. In opposite to the trends at $T_{w,in} = 15.8$ °C, the COP_{plate} trends of $T_{surf} = 35$ °C were slightly higher (5.5%) than the COP_{plate} trends of $T_{surf} = 32.5$ °C at the minimum volume flow rate and it decreased by rising of the volume flow rate at $T_{w,in} = 24.6$ °C. The reason for opposite trends at $T_{w,in} = 15.8$ °C and $T_{w,in} = 24.6$ °C was the impact of the inlet water temperature on the COP_{plate} trends along the experimental period. To better point out, Fig. 7b projected the dynamic COP_{plate} trends at $T_{w,in} = 15.8$ °C and $T_{w,in} = 24.6$ °C at different volume flow rates along the experimental period. It can be seen that the COP_{plate} trends continuously increased from the beginning of the experiments to the end for all volume flow rates at $T_{w,in} = 15.8$ °C because the temperature difference between the inlet water temperature and the cavity wall temperature was high. The absorbed heat rate via water circulation was high enough to keep the COP_{plate} trends increasing and therefore the calculated mean COP_{plate} value for $T_{surf} = 32.5$ °C became greater than the mean COP_{plate} value for $T_{surf} = 35.0$ °C. On the other hand, at $T_{w,in} = 24.6$ °C, the temperature difference between the inlet water temperature and the cavity wall decreased over time and the decreasing temperature resulted in decrement of the absorbed heat rate after a while. Hence, when the target surface temperature decreased from 35.0 °C to 32.5 °C, the mean COP_{plate} value became slightly lower. Fig. 7c shows the mean COP_{system} values at different flow rates and the inlet temperatures. As highlighted in Eq. 11, taking the required cooling rate of the water inlet into the COP calculation increased the consumed energy rate in the denominator; thus, the COP_{system} values at $T_{w,in} =$

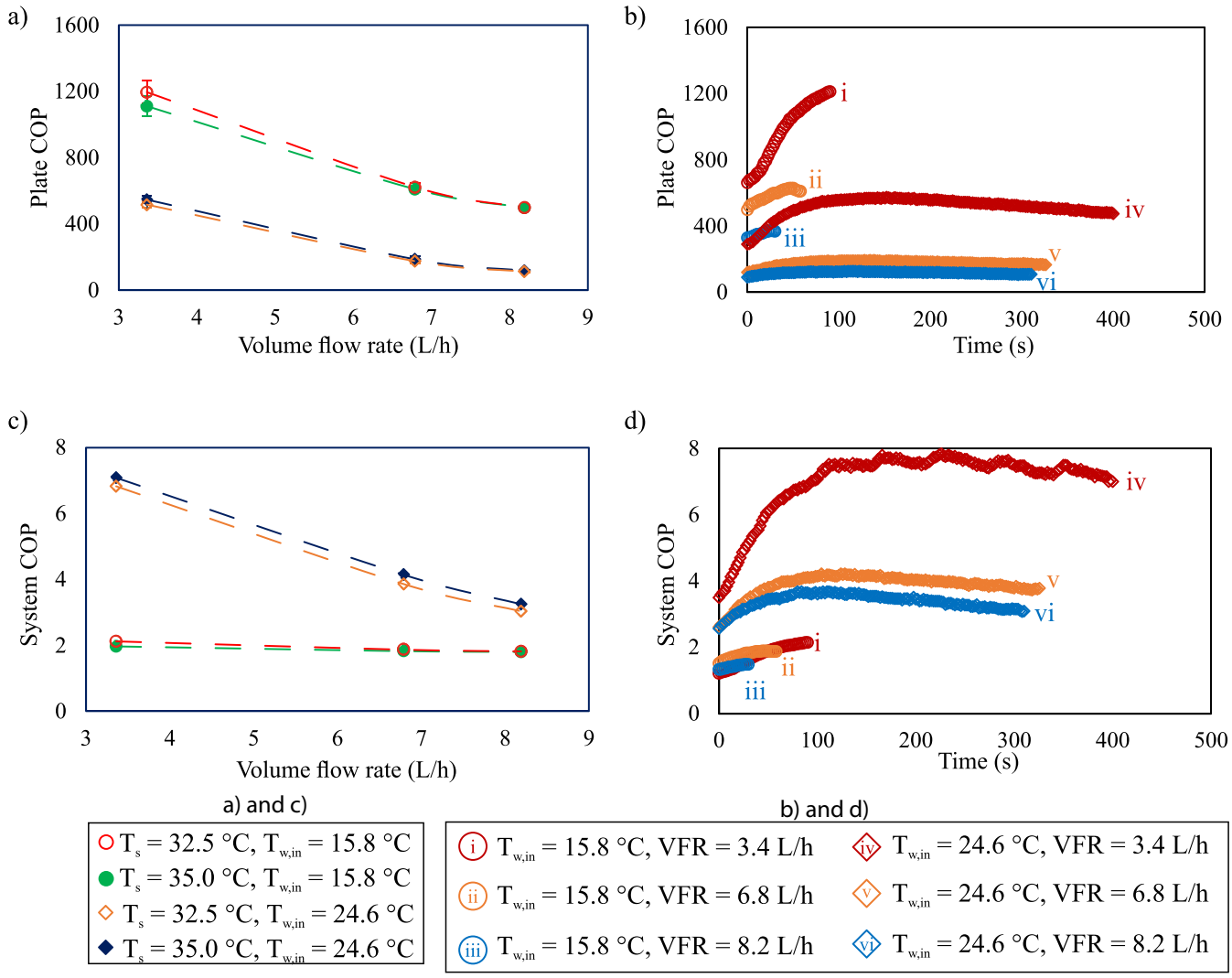

Fig. 7. COP trends of the BCC-filled plate; a) mean COP_{plate}, b) COP_{plate} trends along the experiment period for a selected experiment, c) mean COP_{system}, b) COP_{system} trends along the experiment period for a selected experiment.

15.8 °C became dramatically lower than the $COPs_{system}$ values at $T_{w,in}$ = 24.6 °C. From the volume flow rate of 3.4 L/h to 8.2 L/h, the mean COP_{system} varied decreased from approximately 2.10 to 1.80 at $T_{w,in}$ = 15.8 °C. Nevertheless, the decrease of the mean COP_{system} values was more remarkable from the volume flow rate of 3.4 L/h to 8.2 L/h for operations at $T_{w,in}$ = 24.6 °C. Since the volume flow rate of 3.4 L/h had the minimum pressure drop value, the mean COP_{system} values were found 7.08 and 6.82 for the target surface temperatures of 35.0 °C and 32.5 °C, respectively. At the volume flow rate of 8.2 L/h, the mean COP_{system} values were found nearly 55.0% lower compared to the mean COP_{system} values at the volume flow rate of 3.4 L/h. Similar to the COP_{plate}, the dynamic COP_{system} trends can be seen in Fig. 7d. The fluctuations at $T_{w,in}$ = 24.6 °C (especially for the low volume flow rate) were observed due to the used controller in the study; they did not affect the main outcome of this current work. Similar to the trends in Fig. 7b, the COP trends decreased in the cases for $T_{w,in}$ = 24.6 °C after a while as the temperature difference between the cavity wall and the water inlet temperature became smaller over time, which can also be explained with the thermal inertia.

Fig. 8a shows the mean COP_{plate} trends for the pillar-filled plate according to the inlet water temperatures of 15.7 °C and 24.6 °C. The mean values of COP_{plate} had similar trends to the mean values of the BCC-filled plate. Due to the same reason in the BCC-filled plate, the COP_{plate} trends continued to increase along the experiment period at $T_{w,in}$ = 15.7 °C as shown in Fig. 8b. However, the mean COP_{plate} trends for both T_{surf} = 35.0 °C and T_{surf} = 32.5 °C were close to each other; the mean COP_{plate} decrement rate from the volume flow rate of 3.4 L/h to 8.7 L/h were 9.2% and 10.9% for them, respectively. At $T_{w,in}$ = 24.6 °C, the mean COP_{plate} values were very close to each other for T_{surf} = 35.0 °C and T_{surf} = 32.5 °C since the dynamic COP_{plate} trends at $T_{w,in}$ = 24.6 °C (Fig. 8b) remained almost stable in the late minutes of the experiment period and therefore the mean COP_{plate} did not vary significantly for T_{surf} = 32.5 °C and T_{surf} = 35.0 °C. The mean COP_{plate} decreased by nearly 34.0% from the volume flow rate of 3.4 L/h to 8.7 L/h. The mean values of COP_{system} were presented in Fig. 8c. In parallel to the BCC-filled plate trends, the consideration of the required cooling rate of the inlet water stream dramatically affected the COP trends; hence, the mean COP_{system} values at $T_{w,in}$ = 15.7 °C became lower than the mean COP_{system} values at $T_{w,in}$ = 24.6 °C. When the inlet water temperature was 15.7 °C, the mean COP_{system} was 2.13 and 2.27 at the volume flow rate of 3.4 L/h, but then it decreased to 1.9 and 2.0 at the volume flow rate of 8.7 L/h for T_{surf} = 35.0 °C and T_{surf} = 32.5 °C, respectively. On the other hand, the mean COP_{system} values for T_{surf} = 35.0 °C and T_{surf} = 32.5 °C reached their maximum values of 6.25 and 6.21 at the volume flow rate of 3.4 L/h; then they decreased by 33.38% and 34.58%, respectively, at the volume flow rate of 8.42 L/h when the inlet water temperature was 24.6 °C.

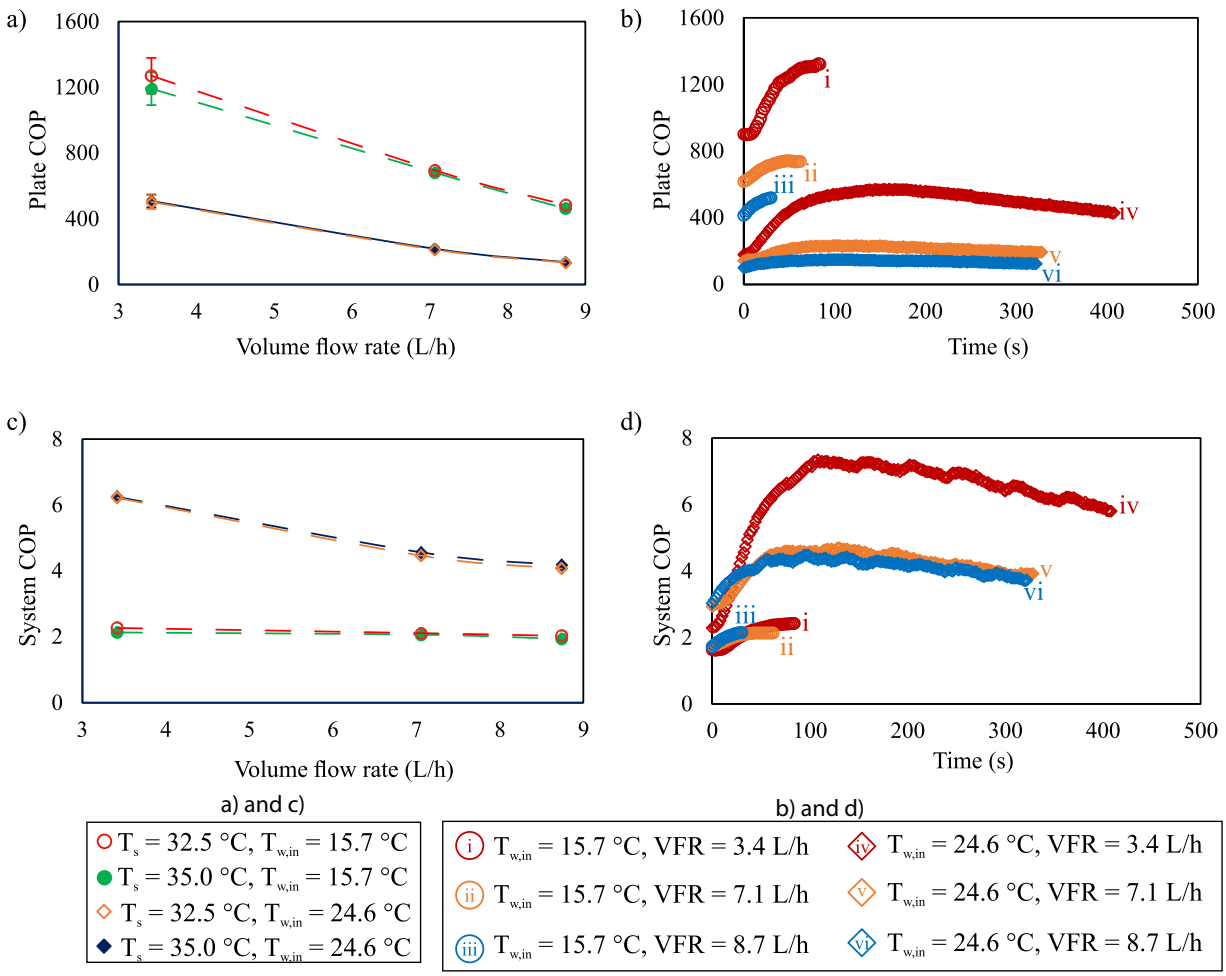

Fig. 8. COP trends of the pillar-filled plate; a) mean COP_{plate}, b) COP_{plate} trends along the experiment period for a selected experiment, c) mean COP_{system}, b) COP_{system} trends along the experiment period for a selected experiment.

Besides the mean COP_{system} values, the dynamic COP_{system} trends of the pillar-filled plate are given in Fig. 8d. Moreover, in the current study, all applied flow rates can be considered low compared to many formerly applied experimental studies in the literature. The results of both plates showed that the pressure drop did not have a significant impact at the low flow rates for the small plate designs when compared to the impact of the required cooling load of the inlet water temperature, which was in good agreement with the results of Li et al. [17], which stated that the pressure drop was negligibly small at low Reynolds numbers, laminar flows.

The average ε trends of the BCC- and pillar-filled plates are presented in Figs. 9a and b, respectively. The ε decreased by rising the volume flow rate in both plates; however, the decrement was more dramatic between the low and medium flow rates. From the medium flow rate to the high flow rate, the decrease of the epsilon can be even neglected since the difference was clearly within the error (bar) range. In Fig. 9a, as the low inlet water temperature achieved a greater temperature difference, the epsilon trends of the low inlet water temperature (15.8 °C) were higher than the epsilon trends of the high inlet water temperature (24.6 °C). The ε difference between the low and high inlet water temperatures also increased with the rising of the volume flow rate. At the flow rate of 3.4 L/h, the epsilon at $T_{w,in}$ = 15.8 °C was 12.6% greater than the ε at $T_{w,in}$ = 24.6 °C whilst it was 46.3% and 52.2% greater at the volume flow rates of 6.8 L/h and 8.2 L/h, respectively. Similar trends were also observed for the pillar-filled plate in Fig. 9b, except for the ε difference between the low and high inlet water temperatures at different flow rates. Unlike the BCC-filled plate, the difference between the low and high inlet water temperatures was nearly the same for all volume flow rates; the low inlet water temperature case had 41.5% greater ε trends than the high inlet water temperature case in all volume flow rates. Moreover, the dynamic changes in the ε trends of the BCC- and pillar-filled plates from the initial surface temperature of 45.0 °C to the target surface temperature of 32.5 °C are shown in Figs. 9c and d, respectively. The plotted dynamic changes presented the same outcome with the mean ε trends when the comparisons were made based on different volume flow rates and the water inlet temperatures. In addition to the ε trends, another criterion can be defined as the thermal resistance (R) between the plate surface (T_s) and the water inlet temperature ($T_{w,in}$) considering the dissipated heat rate($\dot{Q}_d$), which can be defined as $R = \frac{T_s - T_{w,in}}{\dot{Q}_d}$. The dynamic changes of the R trends (see Fig. 7) also presented a similar outcome with the ε trends. By rising the volume flow rates and decreasing the water inlet temperatures, the resistance value became smaller in both BCC- and pillar-filled plates.

The heat transfer coefficient trends of the BCC- and pillar-filled plates are shown in Fig. 10. The mean (average) and the dynamic heat transfer coefficient trends of the BCC-filled plate are plotted in Figs. 10a and b, while the mean and the dynamic trends of the pillar-filled plate are shown in Figs. 10c and d, respectively. In all cases, the h_w increased by rising of the volume flow rate, which was an expected point in parallel to the decrease in cooling times (in Figs. 5 and 6). In Fig. 10a, the h_w had a slight increment, from 118.4 W/m^{2}K to 129.9 W/m^{2}K when the flow rate increased from 3.4 L/h to 8.2 L/h at $T_{w,in}$ = 24.6 °C. However, at $T_{w,in}$ = 15.8 °C, the h_w had a very sharp increment from 141.9 W/m^{2}K to

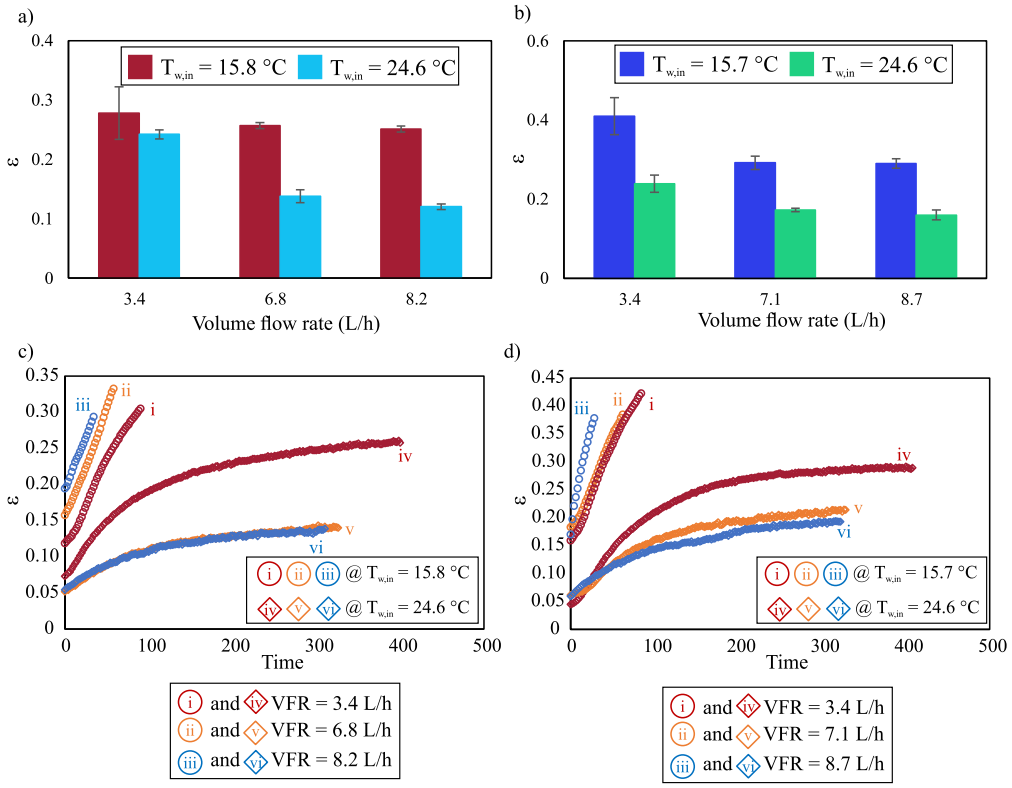

Fig. 9. ε trends of the cold plates at different flow rates, a) mean ε trends of the BCC-filled plate, b) a) mean ε trends of the pillar-filled plate, c) dynamic ε changes of the BCC-filled plate, and d) dynamic ε changes of the pillar-filled plate.

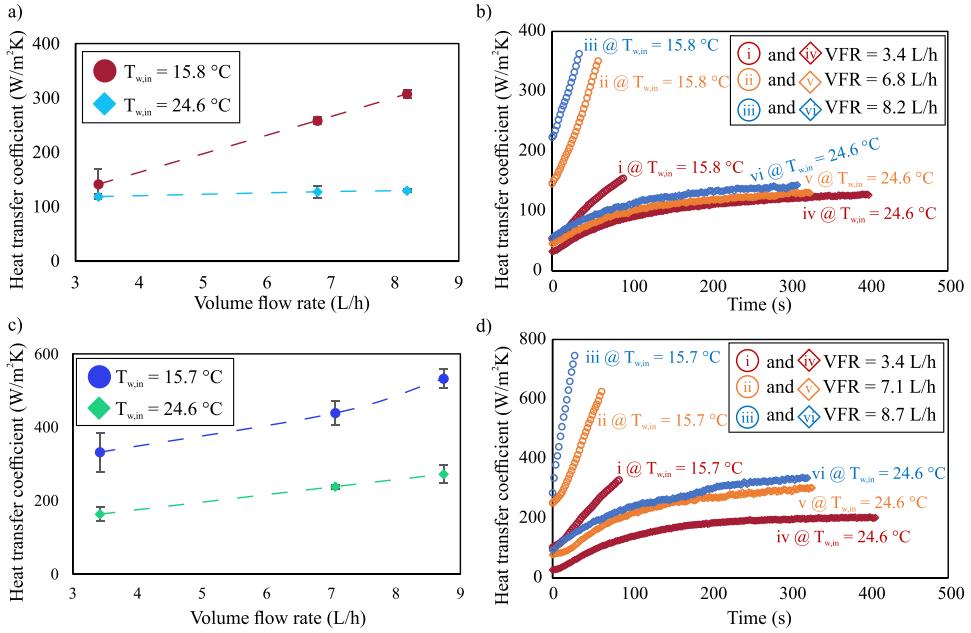

Fig. 10. h_w trends of the cold plates at different flow rates, a) mean h_w trends of the BCC-filled plate, b) dynamic h_w changes of the BCC-filled plate, c) mean h_w trends of the pillar-filled plate, and d) dynamic h_w changes of the pillar-filled plate.

307.4 W/m^{2}K, which nearly corresponded to an increment of 2.16 times. Due to the sharp and slight increments at $T_{w,in} = 15.8$ °C and $T_{w,in} = 24.6$ °C, respectively, the main driving force behind the changes in cooling time trends (Fig. 5) can be understood.The observed outcomes from the mean values can be better recognized by using the dynamic changes in Fig. 10b. Besides, Fig. 10c presents the h_w trends of the pillar-filled plate. Like in the BCC-filled plate trends, the h_w increased by rising the volume flow rate, but the increase at $T_{w,in} = 24.6$ °C was clearer. Also, the pillar-filled plate achieved higher h_w trends at both low and high inlet water temperatures; therefore, the cooling time trends (Fig. 6) were observed greater for the pillar-filled plate. From the volume flow rate of 3.4 L/h to 8.7 L/h, the h_w increased by 1.6–1.7 times at both high and low inlet water temperatures. Similarly, the dynamic changes of the heat transfer coefficients of the pillar-filled plate are projected in

Fig. 10d. The obtained results for the BCC- and pillar-filled plates actually supported the above-mention speculation about the positive impact of laminar vortex shedding behind the pillar elements in the laminar flow; hence, the pillar filled plates showed higher h_w trends.

Fig. 11 shows the VGFs of the experimental data according to the plate type, inlet water temperature and the volume flow rate. It was seen that the $E\beta$ trends increased by rising of the volume flow rate, which was expected due to the increase in the f term. Since the applied flow rates of the pillar-filled plate were slightly higher at the medium and high flow rate levels, the $E\beta$ trends were seen higher than the BCC-filled plate, and therefore a fair comparison between the pillar- and BCC-filled plates would not be sharply accurate. However, it is worth mentioning that the $\eta_0 h_w \beta$ trends of the pillar-filled plate were found greater than the BCC-filled plate, which was parallel to the obtained results in the cooling time and the heat transfer coefficient trends in Figs. 5, 6, and 10. On the other hand, at the low flow rate level, the applied flow rates of both plates were the same; therefore, a basic comparison can be made based on the $E\beta$ and $\eta_0 h_w \beta$ trends. At $T_{w,in} = 24.6$ °C, the BCC-filled plate had a slightly higher $\eta_0 h_w \beta$ value than the pillar-filled plate, but the pillar-filled plate reached a much higher $\eta_0 h_w \beta$ value at $T_{w,in} = 15.8$ °C, which was also in parallel to the discussions of Figs. 5, 6, and 10.

The PEC trends are presented in Fig. 12. On the top-left corner, it was seen that the pillar-filled plate had higher PEC trends than the BCC-filled at all flow rate levels and inlet water temperatures. When the PEC results are compared to the previous works in the literature [21,22,39–43], it is seen that both BCC-filled plate and the pillar-filled plate were in an acceptable region, but the pillar-filled plate had a higher PEC values. It is important to state that the listed previous works in Fig. 12 were not performed at the same conditions from the standpoints of flow rate, coolant inlet temperature, or heat transfer surface area, but they were applied for similar heat load values from the heat sources for the BTMS applications. However, it is a fact that the suggested supporting elements in a cooling cavity gave satisfactory PEC results even though they were operated at very low flow rates and challenging ambient conditions. Compared to the foam structures in the cooling cavity, the supporting elements achieved less pressure drops while they provided enhanced heat transfer rates. Also, it is required to infer that the PEC is not a final decision parameter but a useful performance indicator.

In light of the following discussions, further insights can be discussed with current and possible limita-tions and constraints. The current methodology relied on the collected data on the outer surfaces and the inlet/outlet streams of the cold plate. Based on the data, a one-dimensional heat transfer model was performed without focusing on the thermal inertia and the undefined temperature distribution along the supporting elements well. That is, the current study mainly focused on the plate-level assessment of performance indicators like the cooling time, COP, PEC, and VGF. However, due to the lack of focus on thermal inertia and undefined temperature distribution along the supporting elements, we were not able to make generalized comments on the heat transfer characteristics along the flow pathway in the cooling cavity. To do that, in the near future works, more intensive parametric efforts should be per-formed for the supporting element, cavity design (and dimensions), inlet parameters (temperature and the volume flow rate), and the heat flux from the heat source to the plate. To this end, it can be said that the current study presented thermal performance results for a case study but was not able to gen-eralize the outcomes for different operating conditions. Considering the manufacturing flexibilities of the 3D printing processes, there is still a large research gap on this point.

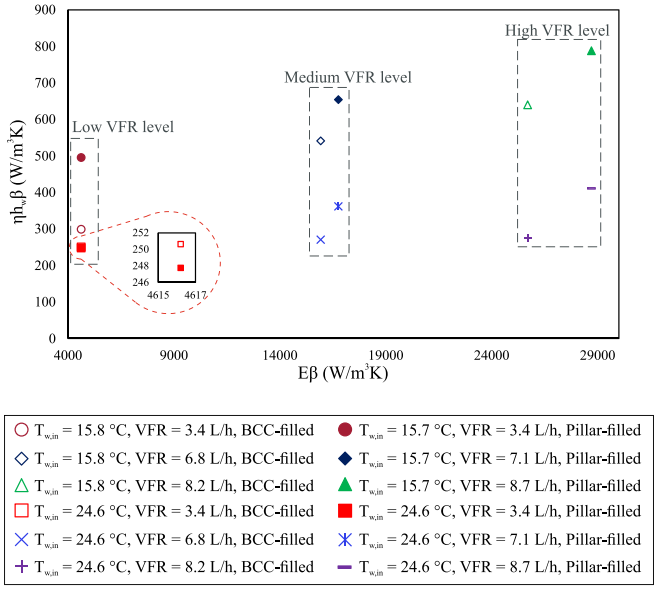

Fig. 11. VGF trends of the BCC- and pillar-filled plates.

6. Conclusion

The presented study experimentally investigated the cooling performance of a metal additive manufactured cold plates with two different supporting elements that were BCC and pillar. The heated surface of the lab-scale setup had an initial surface temperature of 45 °C; then its surface temperature decreased to a target temperature of 32.5 °C under the tropical operating conditions with high ambient air temperature and high relative humidity. The main conclusions are as follows:

- For the BCC-filled plate, the operation with the volume flow rate of 6.8 L/h was observed as the best choice whilst the pillar-filled plate had the shortest cooling time at the highest flow rate of 8.7 L/h.
- In spite of better cooling performance, low inlet temperature cases resulted in a condensation layer, which transiently occurred on the cold plate surface, as the top surface of the setup was in direct contact with the tropical ambient conditions.
- Even though the BCC-filled plate had a greater heat transfer surface area, the cooling time was found shorter in the pillar-filled plate at the low volume flow rate. The laminar vortex shedding behind the pillar elements might be the main reason.
- The mean COP_{plate} range of the pillar-filled plate had close range; 483 to 1270 and 133 to 502 at the low and high inlet water temperatures. The range of the mean COP_{system} was 1.8 to 2.1 and 2.0 to 2.3 for the BCC- and pillar-filled plates at the low inlet water temperature, respectively. At the high inlet water temperature, the mean COP_{system} varied between 3.0 and 7.0 and 4.1 and 6.2 for the BCC- and pillar-filled plates, respectively.
- The epsilon trends decreased by rising the volume flow rate in both BCC- and pillar-filled plates. The range of the epsilon was 0.25 to 0.27 and 0.29 to 0.41 for the BCC- and pillar-filled plates at the low inlet water temperature, respectively. The epsilon trends were smaller at the high inlet water temperature; which were in the range of 0.12 to 0.24 and 0.16 to 0.24 for the BCC- and pillar-filled plates, respectively.
- Compared to the high inlet water temperature, the heat transfer coefficient increased sharply at the low inlet water temperature case by the rising of the volume flow rate. The heat transfer coefficient increased from 141.9 W/m^{2}K to 307.4 W/m^{2}K and from 332.29 W/m^{2}K to 532.7 W/m^{2}K for the BCC- and pillar-filled plates, respectively.
- At the low flow rate level, the BCC-filled plate had slightly better VGF trends than the pillar-filled plate at the low inlet water temperature, but the pillar-filled plate performed better VGF trends at the high inlet water temperature level. Also, the PEC range of the pillar-filled plate was 2.12 to 2.52 whereas the BCC-filled plate had a PEC range of 1.25 to 1.28. Both plates showed better PEC trends than the foam-filled cold plates.

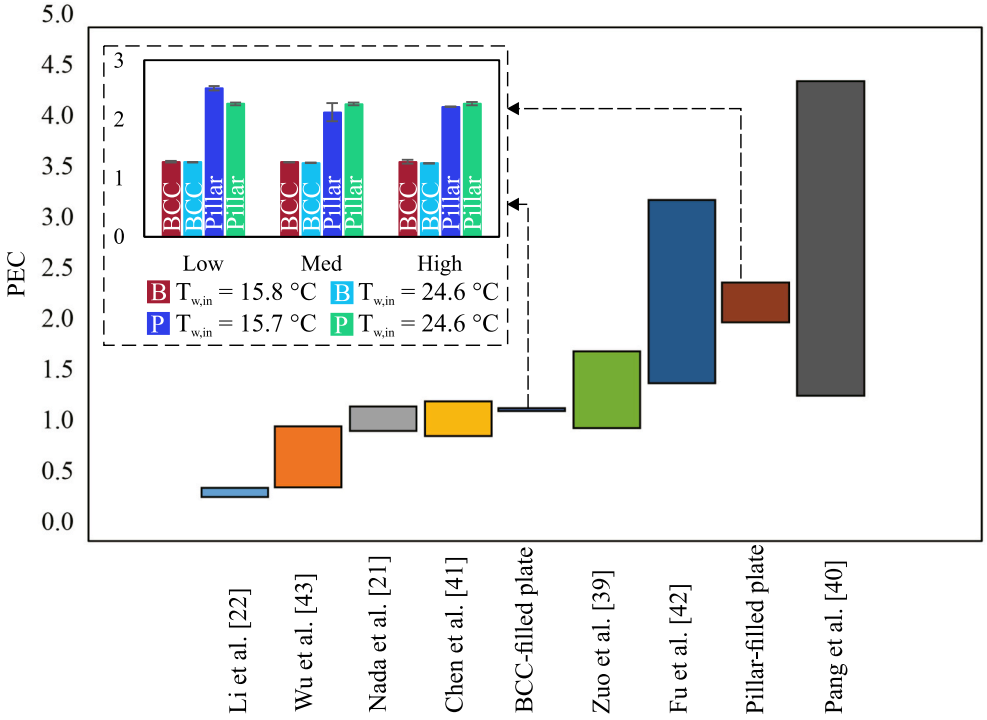

Fig. 12. Comparison of the PEC values with some of the existing cold plate studies.

Regarding the concluded remarks, the near future works can focus on the parametric and multi-criteria decision-making studies to investigate the cooling performance of the metal additive-manufactured plates with various heating loads, initial surface temperatures, flow rates, inlet water temperatures, and hybrid air/liquid cooling scenarios. Also, different metal powders (e.g. aluminum, copper) and plate designs can be studied according to the limitations of the metal additive manufacturing machines.

CRediT authorship contribution statement

Baris Burak Kanbur: Conceptualization, Methodology, Software, Validation, Formal analysis, Investigation, Resources, Data curation, Writing – original draft, Writing – review & editing, Visualization, Supervision, Project administration, Funding acquisition. **Mun Hoe Seat:** Validation, Formal analysis, Investigation, Data curation. **Wiebke Brix Markussen:** Writing – original draft, Writing – review & editing, Supervision. **Martin Ryhl Kærn:** Formal analysis. **Fei Duan:** Writing – original draft, Writing – review & editing, Supervision, Funding acquisition.

Declaration of Competing Interest

The authors declare the following financial interests/personal relationships which may be considered as potential competing interests:

Fei Duan reports financial support was provided by Government of Singapore Ministry of Education. Baris Burak Kanbur reports financial support was provided by Momental Foundation.

Data availability

Data will be made available on request.

Acknowledgement

This study is funded by the Ministry of Education Tier 1 RG154/19 and the Unfettered Research Grant of the Momental Foundation, USA. B. B. Kanbur was the Mistletoe Research Fellow (2020−2021) and sincerely thanks the Momental Foundation for this opportunity during the tough research period in pandemics. We greatly appreciate Mr. Lim Si Xian and Mr. Yi Zhou for their helps to print and characterize the cold plates. The authors would also like to thank the support of the Energy Systems Lab in the School of Mechanical and Aerospace Engineering at Nanyang Technological University (Singapore), the Thermal Energy Section in the Department of Mechanical Engineering at the Technical University of Denmark (Denmark), and the Singapore Centre for 3D Printing (SC3DP) at Nanyang Technological University (Singapore).

Appendix A. Thermal resistance trends of a) BCC-filled plate and b) pillar-filled plate at different volume flow rates and water inlet temperatures

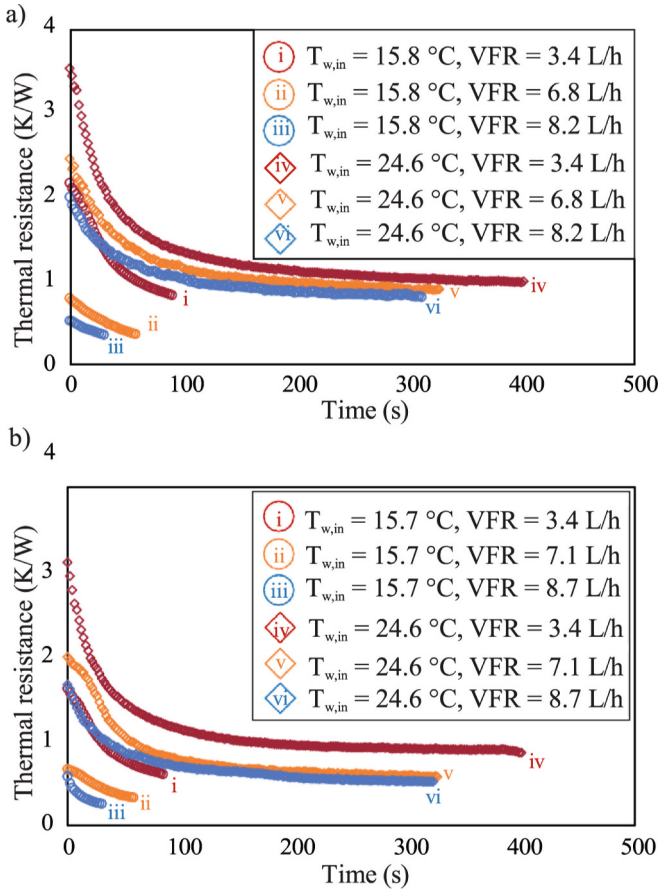

References

[1] F. Zhang, B. Liang, Y. He, H. Gou, Y. Zhu, F. Lu, K. Xiao, Study on flow and heat transfer characteristics of phase change synergistic combination finned liquid cooling plate, Int. Commun. Heat Mass Transf. 138 (2022) 106377.

[2] J. Kim, J. Oh, H. Lee, Review on battery thermal management system for electric vehicles, Appl. Therm. Eng. 149 (2019) 192–212.

[3] S.A. Khan, C. Eze, K. Dong, A.R. Shahid, M.S. Patil, S. Ahmad, I. Hussain, J. Zhao, Design of a new optimized u-shaped lightweight liquid-cooled battery thermal management system for electric vehicles: a machine learning approach, Int. Commun. Heat Mass Transf. 136 (2022) 106209.

[4] X. Yang, T. Liu, W. Yan, S. Wang, Design, fabrication and heat transfer performance study of a novel flexible flat heat pipe, Int. Commun. Heat Mass Transf. 142 (2023) 106673.

[5] K. Xiong, S. Wang, Design, fabrication and characterization of porous ceramics secondary wick of a loop heat pipe to reduce heat leakage, Int. Commun. Heat Mass Transf. 141 (2023) 106582.

[6] D. Xu, Y. Fang, L. Hu, W. Yang, L. Su, Experimental investigation on thermal performance of a pumped two-phase battery cooling system using mini-channel cold plate, Int. J. Energy Res. 45 (2021) 16078–16090.

[7] Q. Ren, H. Yu, Y. Liu, Z. Wang, The investigation of the silicon fabricated balanced shunt micro pin fins cold plate for high heat flux devices, in: 2020 19th IEEE Intersociety Conference on Thermal and Thermomechanical Phenomena in Electronic Systems (ITherm), 2020, pp. 950–956, https://doi.org/10.1109/ITherm45881.2020.9190295.

[8] D. Zhao, Z. Lei, C. An, Research on battery thermal management system based on liquid cooling plate with honeycomb-like flow channel, Appl. Therm. Eng. 218 (2023) 119324.

[9] X. Li, H. Wu, Y. Hu, H. Liu, Y. Yu, K. Huang, Z. Zhang, B. Xue, Y. Gong, Assessing the environmental benefits of battery packs from multi-vehicle and multi-region perspective: aiming for lightweight and carbon neutrality, Environ. Prog. Sustain. Energy 41 (2022), e13892.

[10] J.S. Yang, J.K. Min, C. Yang, K. Jung, Numerical study of natural convection heat transfer of vertical cylinder with multiple lateral baffles in square enclosure for sodium beta-alumina batteries, Int. Commun. Heat Mass Transf. 134 (2022) 106037.

[11] Z. Tang, C. Qi, Z. Tian, L. Chen, Thermal management of electronic components based on new wave bio-inspired structures and nanofluids, Int. Commun. Heat Mass Transf. 131 (2022) 105840.

[12] T. Wang, X. Zhang, Q. Zeng, K. Gao, S. Jiang, Bidirectional heat transfer characteristics of cavity cold plate battery thermal management system: An experimental study, Appl. Therm. Eng. 120242 (2023).

[13] H. Ma, L. Su, B. He, D. He, Y. Kang, New design of u-turn type minichannel cold plate with hybrid fins for high temperature uniformity, Int. Commun. Heat Mass Transf. 135 (2022) 106078.

[14] A. Salimi, M. Khoshvaght-Aliabadi, S. Rashidi, On thermal management of pouch type lithium-ion batteries by novel designs of wavy minichannel cold plates: comparison of co-flow with counter-flow, J. Energy Stor. 52 (2022) 104819.

[15] R. Sun, Q. Fu, G. Chen, Y. Li, S. Wang, J. Zhang, Y. Fan, Y. Xia, N. Ahuja, A novel concept methodology of in-direct cold plate liquid cooling design for data center in cpu socket area, in: 2020 19th IEEE Intersociety Conference on Thermal and Thermomechanical Phenomena in Electronic Systems (ITherm), 2020, https://doi.org/10.1109/ITherm45881.2020.9190567, pp. 471–421.

[16] N.I. Om, R. Zulkifli, P. Gunnasegaran, Influence of the oblique fin arrangement on the fluid flow and thermal performance of liquid cold plate, Case Stud. Thermal Eng. 12 (2018) 717–727.

[17] H. Li, X. Ding, D. Jing, M. Xiong, F. Meng, Experimental and numerical investigation of liquid-cooled heat sinks designed by topology optimization, Int. J. Therm. Sci. 146 (2019) 106065.

[18] O. Kalkan, A. Celen, K. Bakirci, A.S. Dalkilic, Experimental investigation of thermal performance of novel cold plate design used in a li-ion pouch-type battery, Appl. Therm. Eng. 191 (2021) 116885.

[19] J. Cao, Y. He, J. Feng, S. Lin, Z. Ling, Z. Zhang, X. Fang, Mini-channel cold plate with nano phase change material emulsion for li-ion battery under high-rate discharge, Appl. Energy 279 (2020) 115808.

[20] M. Akbarzadeh, T. Kalogiannis, L. Jin, D. Karimi, J. Van Mierlo, M. Berecibar, Experimental and numerical thermal analysis of a lithium-ion battery module based on a novel liquid cooling plate embedded with phase change material, J. Energy Stor. 50 (2022) 104673.
[21] S.A. Nada, R. El-Zoheiry, M. Elsharnoby, O. Osman, Enhancing the thermal performance of different flow configuration minichannel heat sink using al2o3 and cuo-water nanofluids for electronic cooling: An experimental assessment, Int. J. Therm. Sci. 181 (2022) 107767.
[22] Y. Li, L. Gong, B. Ding, M. Xu, Y. Joshi, Thermal management of power electronics with liquid cooled metal foam heat sink, Int. J. Therm. Sci. 163 (2021) 106796.
[23] M. Al-Zareer, Numerical study of flow and heat transfer performance of 3d-printed polymer-based battery thermal management, Int. J. Heat Mass Transf. 158 (2020) 119995.
[24] C.B. Dokken, B.M. Fronk, Optimization of 3d printed liquid cooled heat sink designs using a micro-genetic algorithm with bit array representation, Appl. Therm. Eng. 143 (2018) 316–325.
[25] X. Meng, S. Tan, Z. Yuan, Y. Zhang, L. Chen, Experimental study on the heat transfer performance of a vapour chamber with porous wick structures printed via metallic additive manufacturing, Int. Commun. Heat Mass Transf. 140 (2023) 106496.
[26] B.B. Kanbur, Y. Zhou, S. Shen, K.H. Wong, C. Chen, A. Shocket, F. Duan, Metal additive manufacturing of plastic injection molds with conformal cooling channels, Polymers 14 (2022).
[27] B.B. Kanbur, Y. Zhou, M. Seat, M. Kærn, W.B. Markussen, F. Duan, High-temperature cooling via metal 3d-printed cold plates for battery thermal management, in: International Conference on Materials and Energy (ICOME 2022) ; Conference date: 22-05-2022 Through 25-05-2022, 2022.
[28] D. Liang, G. He, W. Chen, Y. Chen, M.K. Chyu, Fluid flow and heat transfer performance for micro-lattice structures fabricated by selective laser melting, Int. J. Therm. Sci. 172 (2022) 107312.
[29] J. Schindelin, I. Arganda-Carreras, E. Frise, V. Kaynig, M. Longair, T. Pietzsch, S. Preibisch, C. Rueden, S. Saalfeld, B. Schmid, J.-Y. Tineves, D.J. White, V. Hartenstein, K. Eliceiri, P. Tomancak, A. Cardona, Fiji: an open-source platform for biological-image analysis, Nat. Methods 9 (2012) 676–682.
[30] J. Cheng, S. Shuai, Z. Tang, T. Changfa, Thermal performance of a lithium-ion battery thermal management system with vapor chamber and minichannel cold plate, Appl. Therm. Eng. 222 (2023) 119694.
[31] W. Jiang, J. Zhao, Z. Rao, Thermal performance enhancement and prediction of narrow liquid cooling channel for battery thermal management, Int. J. Therm. Sci. 171 (2022) 107250.
[32] R.J. Moffat, Describing the uncertainties in experimental results, Exp. Thermal Fluid Sci. 1 (1988) 3–17.
[33] A.K. Thakur, R. Prabakaran, M. Elkadeem, S.W. Sharshir, M. Arıcı, C. Wang, W. Zhao, J.-Y. Hwang, R. Saidur, A state of art review and future viewpoint on advance cooling techniques for lithium–ion battery system of electric vehicles, J. Energy Stor. 32 (2020) 101771.
[34] F. Ladeinde, A. Muley, M. Stoia, G. Ek, K. Alabi, W. Li, Experimental measurements and mathematical modeling of cold plate for aviation thermal management, Int. J. Heat Mass Transf. 191 (2022) 122810.
[35] R.K. Shah, D.P. SekuliÂ, Basic Thermal Design Theory for Recuperators, John Wiley & Sons, Ltd, 2003, pp. 97–231, https://doi.org/10.1002/9780470172605.ch3.
[36] R. Shah, A. London, Chapter xvii - discussion—an overview for the designer and the applied mathematician, in: R. Shah, A. London (Eds.), Laminar Flow Forced Convection in Ducts, Academic Press, 1978, pp. 385–420. https://www.sciencedirect.com/science/article/pii/B978012020051150022X. https://doi.org/10.1016/B978-0-12-020051-1.50022-X.
[37] N. Sahiti, F. Durst, A. Dewan, Strategy for selection of elements for heat transfer enhancement, Int. J. Heat Mass Transf. 49 (2006) 3392–3400.
[38] R.L. Webb, N.-H. Kim, Performance evaluation criteria for single-phase flow, Garland Sci. (2004) 55–75, https://doi.org/10.1201/b12413.
[39] W. Zuo, Y. Zhang, J. E, J. Li, Q. Li, G. Zhang, Performance comparison between single s-channel and double s-channel cold plate for thermal management of a prismatic lifepo4 battery, Renew. Energy 192 (2022) 46–57.
[40] X. Pang, Y. Huo, H. Fang, Z. Rao, Analysis of temperature uniformity of electric vehicle battery system with swirling flow strengthened heat transfer, Appl. Therm. Eng. 193 (2021) 116995.
[41] Z. Chen, S. Yang, M. Pan, J. Xu, Experimental investigation on thermal management of lithium-ion battery with roll bond liquid cooling plate, Appl. Therm. Eng. 206 (2022) 118106.
[42] J. Fu, Y. Li, Z. Cao, B. Sundén, J. Bao, G. Xie, Effect of an impinging jet on the flow characteristics and thermal performance of mainstream in battery cooling of hybrid electric vehicles, Int. J. Heat Mass Transf. 183 (2022) 122206.
[43] C. Wu, J. Zhao, C. Liu, Z. Rao, Performance and prediction of baffled cold plate based battery thermal management system, Appl. Therm. Eng. 219 (2023) 119466.
[44] X. Xu, R. He, Research on the heat dissipation performance of battery pack based on forced air cooling, J. Power Sources 240 (2013) 33–41.